



Cite this: *Phys. Chem. Chem. Phys.*, 2024, 26, 24954

# Prediction of ultraviolet optical materials in the $K_2O-B_2O_3$ system†

Xiaoqing Guo,<sup>‡</sup> Yanting Wang<sup>‡</sup> and Haiyang Niu<sup>‡\*</sup>

Ultraviolet (UV) birefringent crystals play a crucial role in various fields, such as laser technologies, optical telecommunications, and advanced scientific instrumentation. Alkali metal borates, with their diverse structures and remarkable ultraviolet optical properties, have garnered significant attention in recent years. In this study, employing the evolutionary crystal structure prediction algorithm USPEX, in conjunction with ionic substitutions and first-principles calculations, we systematically explored the pseudo-binary  $K_2O-B_2O_3$  system and predicted two stable structures (*oP56-K<sub>3</sub>BO<sub>3</sub>* and *mC44-K<sub>4</sub>B<sub>2</sub>O<sub>5</sub>*) previously unreported, and twelve metastable structures in the  $K_2O-B_2O_3$  system. A comprehensive analysis of their structural, electronic and optical properties is conducted. The coplanar arrangement of  $BO_3$  and  $B_3O_6$  groups is found to enhance optical anisotropy, thereby increasing the birefringence. In the  $K_2O-B_2O_3$  system, six structures with wide band gaps and high birefringence (*mP28-1-K<sub>3</sub>BO<sub>3</sub>*, *tR72-KBO<sub>2</sub>*, *oP112-1-KB<sub>5</sub>O<sub>8</sub>*, *oP112-2-KB<sub>5</sub>O<sub>8</sub>*, *mC220-K<sub>5</sub>B<sub>19</sub>O<sub>31</sub>*, and *hR21-K<sub>3</sub>BO<sub>3</sub>*) are found to be possible candidates for UV optical materials. Importantly, *hR21-K<sub>3</sub>BO<sub>3</sub>*, the only non-centrosymmetric structure in this system, exhibits a significant frequency doubling coefficient (about 4.6 KDP) and a moderate birefringence index (0.056@1064 nm), marking it a promising UV nonlinear optical material.

Received 17th June 2024,  
 Accepted 9th September 2024

DOI: 10.1039/d4cp02424a

rsc.li/pccp

## 1 Introduction

Ultraviolet (UV) birefringent crystals, known for their inherent ability to modulate and polarize light, play a crucial role in the optical domain, particularly in scientific instrumentation, advanced optical communication systems, and the ultraviolet laser industry.<sup>1–5</sup> To meet the demands of practical applications, birefringent crystals must meet basic but stringent criteria:<sup>6</sup> substantial birefringence, wide bandgap (corresponding to short UV cutoff edge), high laser-induced damage threshold, facile crystal growth, and excellent physical and chemical stability. These rigorous standards significantly raise the difficulty of discovering UV optical crystal materials with superior performance properties.<sup>7,8</sup> Thus far, UV birefringent crystals predominantly utilized in commercial applications include  $MgF_2$ <sup>9</sup> and  $\alpha-BaB_2O_4$ .<sup>10–12</sup>  $\alpha-BaB_2O_4$  exhibits significant birefringence and a broad transmission range, but it undergoes phase transition and is prone to cracking when growing.  $MgF_2$ , with a short UV cutoff in the deep UV region, has a small birefringence (0.014@193 nm), limiting device miniaturization. Thus, the

development of high-performance birefringent crystals for the UV spectrum is imperative.

In recent years, borate systems have garnered significant interest among researchers due to their diverse structures, wide transmission range, stable physical and chemical properties, and excellent luminescence efficiency.<sup>13,14</sup> Furthermore, alkali metal cations are known for lacking d–d and f–f electron transitions, which enables the extension of the cutoff edge to the ultraviolet or even deep ultraviolet region.<sup>15</sup> Consequently, alkali metal borates are regarded as abundant sources of materials suitable for ultraviolet and deep-ultraviolet optical applications, such as  $\alpha-LiBO_2$ ,<sup>16</sup>  $Li_2Na_2B_2O_5$ ,<sup>17</sup> and  $CsB_4O_6F$ .<sup>18</sup> However, the variety of materials available for ultraviolet birefringent applications remains relatively limited. Therefore, the exploration of novel alkali borate structures holds great significance for the development of potential high-performance ultraviolet optical materials.

Both experimental and theoretical studies have established that alkali metal borate compounds within the Li–B–O system encompass a broad phase space.<sup>19</sup> Despite potassium and lithium being in the same main group of the periodic table, only seven structures in the  $K_2O-B_2O_3$  system have been documented ( $KBO_2$ ,<sup>20,21</sup>  $KB_3O_5$ ,<sup>22</sup>  $HP-KB_3O_5$ ,<sup>23</sup>  $K_2B_4O_7$ ,<sup>24</sup>  $\alpha-KB_5O_8$ ,  $\beta-KB_5O_8$ ,<sup>25,26</sup> and  $K_5B_{19}O_{31}$ <sup>27</sup>), highlighting substantial unexplored potential. Furthermore, although these compounds have been synthesized experimentally, their optical properties have seldom been studied in depth. In 2019, Huang *et al.*

State Key Laboratory of Solidification Processing, International Center for Materials Discovery, School of Materials Science and Engineering, Northwestern Polytechnical University, Xi'an 710072, P. R. China. E-mail: haiyang.niu@nwpu.edu.cn

† Electronic supplementary information (ESI) available. See DOI: <https://doi.org/10.1039/d4cp02424a>

‡ These authors contributed equally to this work.

demonstrated that the  $K_5B_{19}O_{31}$  crystal exhibits a moderate birefringence of 0.05@1064 nm and an ultraviolet cutoff below 180 nm, underscoring its potential as a deep UV birefringent material.<sup>28</sup> These insights emphasize the need for comprehensive research into the structure and properties of the  $K_2O-B_2O_3$  system.

According to the theory of anionic groups,<sup>29,30</sup> the planar units  $[BO_3]^{3-}$  and  $[B_3O_6]^{3-}$  with  $\pi$ -conjugated orbitals can significantly enhance the anisotropy of polarizability, thus favoring higher birefringence, making them excellent structural units for designing short-wavelength birefringent materials.<sup>31</sup> Statistical analyses indicate that the cationic ratio significantly influences the degree of B–O polymerization, with higher K/B ratios facilitating the formation of isolated B–O groups. Notably, the known compounds with relatively low potassium content ( $K/B \leq 1$ ) exhibit complex fundamental building blocks.<sup>28</sup> Therefore, exploring potassium-rich structures in the  $K_2O-B_2O_3$  system holds substantial potential for applications.

In this study, we have employed ion substitutions,<sup>32</sup> evolutionary crystal structure prediction algorithm USPEX,<sup>33–35</sup> and first-principles calculations to explore the configuration space of the pseudo-binary  $K_2O-B_2O_3$  system. Through thermodynamic and dynamic stability analysis, we have successfully predicted two potassium-rich ground state structures (*oP56-K<sub>3</sub>BO<sub>3</sub>* and *mC44-K<sub>4</sub>B<sub>2</sub>O<sub>5</sub>*), as well as twelve thermodynamically metastable structures, thereby enriching the structural database of the borate system. We conducted a systematic analysis of the electronic structures and optical properties of various structures within the entire system, encompassing both predicted and reported structures. Through this analysis, we assessed their potential as optical materials. Among them, *tR72-KBO<sub>2</sub>*, featuring planar  $B_3O_6$  groups, exhibits significant birefringence (0.096@1064 nm and 0.1@564 nm). Especially, *hR21-K<sub>3</sub>BO<sub>3</sub>*, as the only non-centrosymmetric structure, exhibits a considerable frequency doubling coefficient ( $\sim 4.6$  KDP) and a moderate birefringence index (0.056@1064 nm), making it a potential UV nonlinear optical material.

## 2 Computational details

To generate borate structures with high potassium content in the  $K_2O-B_2O_3$  system, we have employed the material programming interface provided by the Materials Project database with Python to carry out data mined ionic substitutions.<sup>36</sup> The valence states of K, B, and O were defined as +1, +3, and –2, respectively. A replacement probability threshold of 0.001 was established for element substitution, with a maximum limit of 500 chemical systems. Through screening, we have identified 108 candidate systems for ion substitutions and collected all relevant crystal structures of these systems from the database. Subsequently, the corresponding elements in the original systems were replaced with K, B, and O, and duplicate and existing structures in the database were filtered out. Finally, the structures with lower energies were selected as the seeds for the subsequent structure search, enhancing the efficiency of crystal structure prediction.

The evolutionary crystal structure prediction algorithm USPEX was performed to explore new structures within the  $K_2O-B_2O_3$  system. Initially, we generated a diverse pool of 180 structures randomly, each containing up to 40 atoms per unit cell. This initial generation served as the basis for subsequent iterations, where 150 structures per generation were produced using the following structural operators: heredity (0.5), random formation (0.2), soft mutation (0.2), and transmutation (0.1). Meanwhile, structural relaxations and energy calculations were conducted using the Vienna ab initio Simulation Package (VASP) code.<sup>37</sup> This involved employing the projected augmented-wave (PAW) method<sup>38</sup> coupled with the generalized gradient approximation (GGA) based on the Perdew–Burke–Ernzerhof (PBE) exchange–correlation density functional.<sup>39</sup> The electron–ion interactions were described using PAW potentials with  $4s^1$ ,  $2s^22p^1$ , and  $2s^22p^4$  valence electrons for potassium, boron, and oxygen, respectively. To achieve precise relaxation, we conducted five stages of structural relaxation on each structure, with an energy cutoff of 500 eV for each stage. The resolution of the k-point grid in reciprocal space was progressively set at  $2\pi \times 0.12 \text{ \AA}^{-1}$ ,  $2\pi \times 0.09 \text{ \AA}^{-1}$ ,  $2\pi \times 0.07 \text{ \AA}^{-1}$ ,  $2\pi \times 0.06 \text{ \AA}^{-1}$ , and  $2\pi \times 0.05 \text{ \AA}^{-1}$ . Following the completion of structure prediction, to further enhance the precision of energy calculations, convergence tests were conducted. The energy cutoff was adjusted to 600 eV, and a  $\Gamma$ -centered mesh with a spacing threshold of  $0.25 \text{ \AA}^{-1}$  was employed.

The formation energies of the compound predicted in the pseudo-binary  $K_2O-B_2O_3$  system are calculated using the following equation,

$$\Delta E \left( K_x B_y O_{\frac{x+3y}{2}} \right) = \frac{E \left( K_x B_y O_{\frac{x+3y}{2}} \right) - \frac{x}{2} E(K_2O) - \frac{y}{2} E(B_2O_3)}{\frac{x+y}{2}} \quad (1)$$

where  $E \left( K_x B_y O_{\frac{x+3y}{2}} \right)$  is the total energy of the predicted structures;  $E(K_2O)$  and  $E(B_2O_3)$  are energies of the corresponding ground state structures of  $K_2O$ <sup>40</sup> and  $B_2O_3$ ,<sup>41</sup> respectively.

The phonon dispersion was calculated using the finite displacement method as implemented in the PHONOPY code.<sup>42</sup> The crystal structures were visualized using the VESTA software.<sup>43</sup> In addition, electronic structures and projected density of states (PDOS) are calculated using the GGA-PBE and HSE06<sup>44</sup> hybrid functional implemented in the VASP code, respectively. The exact exchange fraction is 0.25 in the hybrid functional calculation.

Furthermore, we employed the sum-over-states (SOS) method, as implemented in the first-principles software ABINIT,<sup>45</sup> to compute the optical properties using an Optimized Norm-Conserving Vanderbilt (ONCV) pseudopotential.<sup>46</sup> We set the plane-wave cutoff energy at 40 Ha and employed the scissor operator<sup>47</sup> to accurately adjust the discrepancy between the band gaps. Finally, we use the AbiPy library to analyze the optical properties.

### 3 Results and discussion

#### 3.1 Dynamical and thermodynamic stability of the predicted structures

With extensive exploration of the  $K_2O$ - $B_2O_3$  system, we have determined the thermodynamic convex hull and calculated the formation energies of the sampled structures at 0 K, as illustrated in Fig. 1. In principle, structures located on the convex hull are thermodynamically stable, whereas structures positioned above the convex hull but with negative formation energies are thermodynamically metastable. In agreement with previous experiments, *tR72*- $KBO_2$ ,<sup>20,21</sup> *aP52-1*- $K_2B_4O_7$ ,<sup>24</sup> *mC220*- $K_5B_{19}O_{31}$ ,<sup>27</sup> and *oP112-1*- $KB_5O_8$ <sup>26</sup> are predicted to be stable, indicating the reliability of the methodology we adopted. Importantly, we have also predicted two other stable phases, *oP56*- $K_3BO_3$  and *mC44*- $K_4B_2O_5$ , which have not been reported before. In addition, taking into account the effects of temperature and pressure on phase stability (Fig. S1, ESI<sup>†</sup>), structures that are approximately 0.1 to 0.2 eV per atom above the convex hull can usually be synthesized experimentally.<sup>48,49</sup> Here, we have further calculated the phonon dispersion curves for structures with formation energies less than 0.08 eV f.u.<sup>-1</sup> above the convex hull and predicted twelve thermodynamically metastable and dynamically stable structures, evidenced by the absence of imaginary frequencies in the phonon spectra (Fig. S2, ESI<sup>†</sup>). The detailed crystallographic information and bond valence sum (BVS) values are given in Table S1 (ESI<sup>†</sup>). The calculated valence states are in agreement with ideal valences, indicating the rationality of the predicted structures. The prediction of novel structures not only expands the configuration space of the  $K_2O$ - $B_2O_3$  system, allowing for systematic investigation of structures and properties, but also offers vital insights for the enhancement and design of borate systems.

The fourteen structures predicted comprise three components:  $K_3BO_3$ ,  $K_4B_2O_5$ , and  $K_2B_4O_7$ .  $K_3BO_3$  and  $K_4B_2O_5$  exhibit relatively higher potassium contents. Specifically, for  $K_3BO_3$ , we have predicted eleven distinct structures, each represented by Pearson symbols, listed in Fig. 1b, with energies decreasing sequentially from top to bottom. For  $K_4B_2O_5$ , besides the newly predicted stable structure *mC44*- $K_4B_2O_5$ , *aP22*- $K_4B_2O_5$  is found to be metastable. And for  $K_2B_4O_7$ , we have predicted a metastable structure *aP52-2*- $K_2B_4O_7$  that shares the same Pearson symbol with its ground stable structure *aP52-1*- $K_2B_4O_7$ . Notably, among all the experimental and predicted structures, *hR21*- $K_3BO_3$  is found to be the only non-centrosymmetric structure in the  $K_2O$ - $B_2O_3$  system. In the field of optical crystals, nonlinear optical crystals with non-centrosymmetric structures also play a crucial role alongside birefringent crystals. They are widely utilized, particularly in areas such as laser frequency conversion and electro-optic modulation.<sup>50–53</sup> Therefore, the discovery of the *hR21*- $K_3BO_3$  structure opens new possibilities for the study and development of novel nonlinear optical materials in the K-B-O system, with significant practical value.

Moreover, we noted in the Open Quantum Materials Database (OQMD)<sup>54,55</sup> that six structures of  $K_3BO_3$  were predicted by Schmidt *et al.*<sup>56</sup> using high-throughput screening methods. Nevertheless, our density functional theory (DFT) calculations indicate that the formation energies of these six structures are significantly higher than the eleven  $K_3BO_3$  structures we predicted here. This underscores the necessity of using evolutionary algorithms for structure exploration in specific systems.

#### 3.2 Crystal structures

In this section, we would focus on the crystal structure features of compounds in the  $K_2O$ - $B_2O_3$  system. Representative crystal structures with different compositions are summarized in

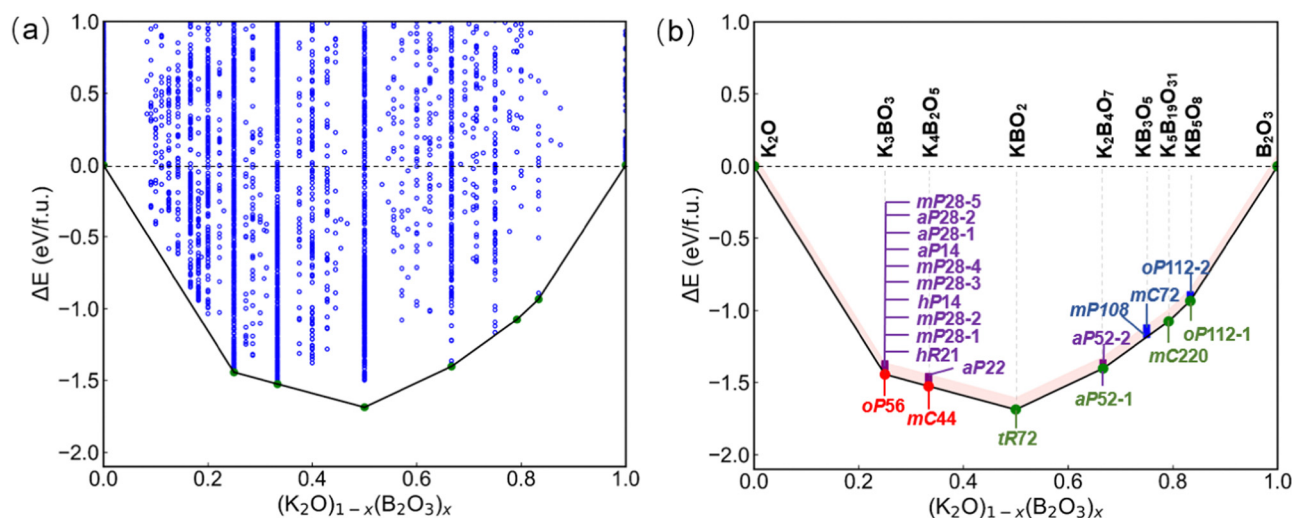


Fig. 1 Thermodynamic convex hull of the  $K_2O$ - $B_2O_3$  system at 0 K. (a) Each circle or dot represents an individual structure. (b) Structures obtained from energy filtering. Thermodynamically stable structures are denoted by solid dots: red for structures predicted in this study and green for those previously reported. Thermodynamically metastable structures are represented by solid squares, with purple indicating new predictions and blue marking previously reported structures.

Fig. 2a. We have annotated the fundamental building blocks of these structures, revealing a noticeable increase in the aggregation tendency of boron–oxygen anions with changing compositions, thereby leading to the development of more complex framework structures.

Among the fourteen predicted structures, the anionic groups can be categorized into three groups, including  $\text{BO}_3$ ,  $\text{B}_2\text{O}_5$ , and  $\text{B}_8\text{O}_{14}$ . It is shown that all structures of  $\text{K}_3\text{BO}_3$  feature zero-dimensional (0D)  $\text{BO}_3$  units, while  $\text{K}_4\text{B}_2\text{O}_5$  exhibits 0D  $\text{B}_2\text{O}_5$  units, and  $aP52\text{-}2\text{-K}_2\text{B}_4\text{O}_7$  is characterized with  $\text{B}_8\text{O}_{14}$  groups. For comprehensive information regarding all predicted structures, please refer to the Table S1 and Fig. S3 (ESI $^\dagger$ ).

All  $\text{K}_3\text{BO}_3$  structures share a common feature of forming a three-dimensional network through K–O bonding. Although each structure has anionic groups of isolate  $\text{BO}_3$ , the internal arrangement of these groups varies. Here, we take the newly predicted ground state structure as an example to explicitly analyze its structure. The  $oP56\text{-K}_3\text{BO}_3$  structure crystallizes as the orthorhombic system with space group  $Pbam$ , and the asymmetric unit contains five potassium atoms, two boron atoms, and four oxygen atoms. We assign labels to atoms based on their local environments. K1, K4, and K5 exhibit hexacoordination with six oxygen atoms, and the K–O bond distance varies within the ranges of 2.8344 to 2.8953 Å, 2.6848 to 3.1292 Å,

and 2.6959 to 3.1882 Å, respectively. K2 and K3 are coordinated with five oxygen atoms, with bond lengths ranging from 2.5141 to 2.9416 Å and from 2.5314 to 3.0741 Å, respectively. B1 and B2 form  $\text{BO}_3$  groups with three oxygen atoms, exhibiting slightly different bond lengths and bond angles. The  $[\text{KO}_5]$  and  $[\text{KO}_6]$  polyhedra are interconnected through shared angles and edges, creating a three-dimensional K–O framework with boron atoms located in the channels.

In addition to  $oP56\text{-K}_3\text{BO}_3$ , we will particularly focus on structures with parallel or nearly parallel arranged  $\text{BO}_3$  groups, such as  $hR21\text{-K}_3\text{BO}_3$  (Fig. 2b) and  $mP28\text{-}1\text{-K}_3\text{BO}_3$  (Fig. 2c). The formation energies of the two structures are very close to the convex hull, only 0.3 meV f.u. $^{-1}$  and 3.6 meV f.u. $^{-1}$  higher, respectively, indicating their high likelihood for synthesis in experiments. The  $hR21\text{-K}_3\text{BO}_3$  structure crystallizes in the trigonal system ( $R3m$ ), and its asymmetric unit contains one potassium atom, one boron atom, and one oxygen atom. The  $\text{BO}_3$  group features equal B–O bond lengths, with the O–B–O bond angles measuring 120°. Internally, the  $\text{BO}_3$  units are perfectly aligned in parallel.  $mP28\text{-}1\text{-K}_3\text{BO}_3$  crystallizes in the monoclinic system ( $P2_1/c$ ). The distances between B and O in the  $\text{BO}_3$  units range from 1.396 to 1.414 Å, while the O–B–O bond angles vary from 119.84 to 120.07°. Adjacent planar  $\text{BO}_3$  groups are approximately parallel, displaying a very small angle.

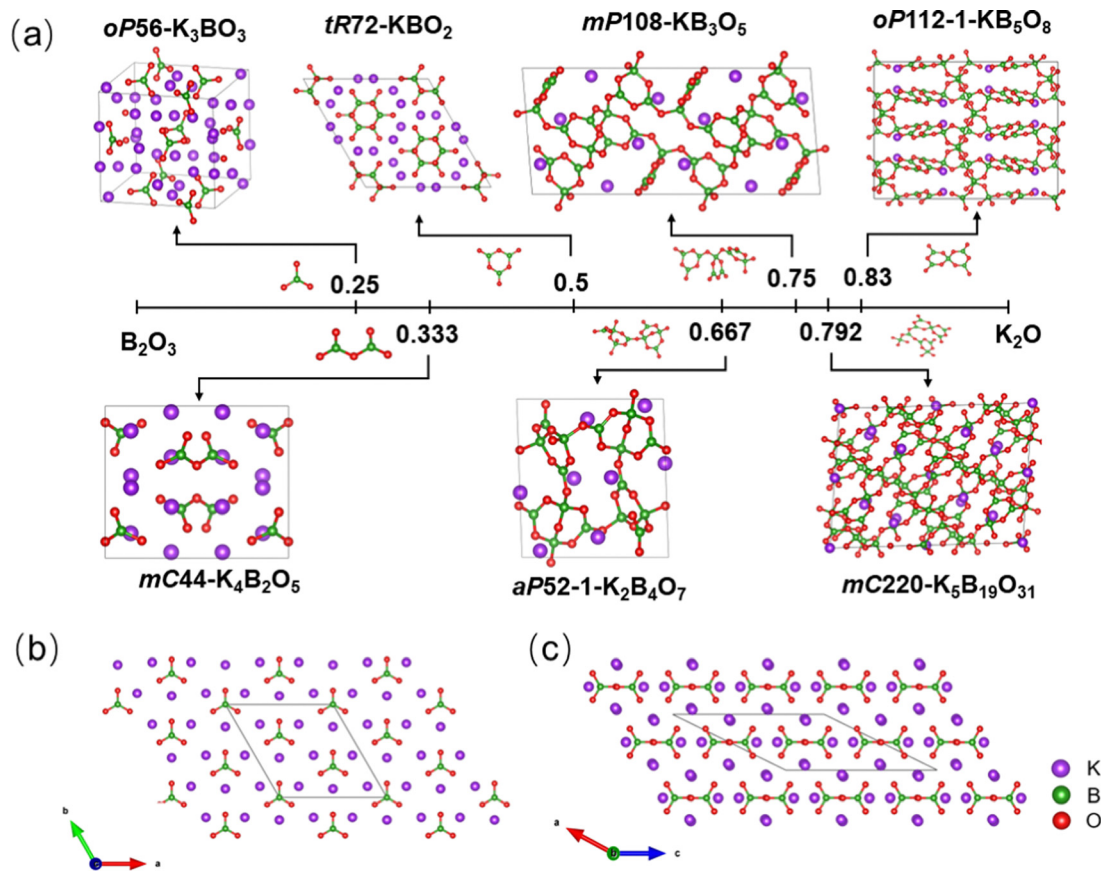


Fig. 2 (a) Structures of varying compositions in the  $\text{K}_2\text{O}$ – $\text{B}_2\text{O}_3$  system. Except for  $mP108\text{-KB}_3\text{O}_5$ , all are ground state structures. The B–O groups forming the crystal structures are indicated in the figure. (b)  $hR21\text{-K}_3\text{BO}_3$ . (c)  $mP28\text{-}1\text{-K}_3\text{BO}_3$ . The unit cell is plotted with solid lines. We disregard the bonding of potassium atoms in order to focus on the analysis of B–O groups.

For  $K_4B_2O_5$ , we focus on the new ground state structure  $mC44-K_4B_2O_5$ . It crystallizes to the  $C2/c$  space group in the monoclinic system. It contains two inequivalent potassium atoms, three inequivalent oxygen atoms, and a unique boron atom. K1 is coordinated by five oxygen atoms with K–O distances ranging from 2.6698 to 2.8427 Å, and K2 is coordinated by six oxygen atoms with K–O distances ranging from 2.6918 to 3.5708 Å. B1 combines with three oxygen atoms to form the  $BO_3$  group, with bond lengths ranging from 1.3732 to 1.4562 Å and O–B–O bond angles between 117.42 and 124.05°. Two  $BO_3$  planar groups with an acute angle are further connected through shared oxygen atoms to form a  $B_2O_5$  group.  $[KO_5]$  and  $[KO_6]$  polyhedra are interconnected alternately through edges and vertices to form a three-dimensional structure.

When the  $K_2O:B_2O_3$  ratio is 1:1,  $KBO_2$  is characterized by unique 0D  $B_3O_6$  rings. These planar rings are formed by the aggregation of three  $BO_3$  triangles sharing common oxygen atoms, and are arranged in parallel within the crystal structure. It is noteworthy that we did not observe one-dimensional (1D)  $[BO_2]_\infty$  chain structures similar to  $LiBO_2$ <sup>16</sup> or  $Ca(BO_2)_2$ <sup>6</sup> within this system. The larger radius of monovalent potassium ions tends to promote the formation of rings, thereby mitigating interionic repulsion and maintaining the stability of the crystal structure.

As the chemical portion of  $B_2O_3$  increases, boron atoms predominate in the cations, displaying a four-coordination with oxygen atoms to form  $BO_4$  tetrahedra, which facilitates spatial connectivity and increases the polymerization of six-membered ring structures. Taking structures in Fig. 2 as examples, we will focus on these basic polyanion structural units. The fundamental building block of  $aP52-1-K_2B_4O_7$  consists of a  $BO_3$  triangle, a  $B_3O_8$  ring, and a shared edge  $B_4O_{13}$  double ring, with a  $K_2O:B_2O_3$  ratio of 1:2. In contrast,  $aP52-2-K_2B_4O_7$  (Fig. S3j, ESI†) is a predicted thermodynamically metastable structure featuring  $B_8O_{14}$  groups that differ from the ground

state structure. The  $B_8O_{14}$  group is composed of a  $B_5O_{11}$  double ring and a  $B_3O_7$  ring. The anionic basic unit of  $mP108-KB_3O_5$  ( $K_2O:B_2O_3 = 1:3$ ) consists of three  $B_3O_7$  rings interconnected by oxygen atoms, with each ring formed by the aggregation of two  $BO_3$  triangles and one  $BO_4$  tetrahedron. When the  $K_2O:B_2O_3$  ratio is 5:19, the crystal structure of  $K_5B_{19}O_{31}$  has the most complex fundamental building block. A  $BO_4$  tetrahedron, a  $B_3O_7$  ring, a  $BO_3$  triangle, and a  $B_5O_{10}$  double ring, together with half a tetrahedron, are interconnected *via* oxygen atoms. Then by applying reflection symmetry about the quadratic axis, a  $B_{19}O_{35}$  unit is formed. Both structures of  $KB_5O_8$  ( $K_2O:B_2O_3 = 1:5$ ) crystallize in the  $Pbca$  space group and feature identical  $B_5O_{10}$  double rings shared by common boron atoms. However, the two structures differ in the torsion angles between interconnected double rings internally. The impact of these complex anionic building blocks on the optical properties of crystals requires further investigation.

Moreover, in the  $K_2O-B_2O_3$  system, there is a noted trend indicating that the average coordination number of potassium atoms tends to rise with the increasing  $B_2O_3/K_2O$  ratio in the ground state structures (Fig. 3a). In the predicted potassium-rich structures ( $x = 0.25$  and 0.33), both the stable and metastable configurations exhibit average coordination numbers approximately ranging from five to six. With the decrease in potassium content, the K–O bond lengths increase, and the coordination numbers in the ground state structures are approximately between seven and eight. It is noteworthy that some metastable structures exhibit higher or lower coordination numbers, such as  $aP52-2-K_2B_4O_7$  (5.5),  $mC72-KB_3O_5$  (5), and  $oP112-2-KB_5O_8$  (10). For the  $mP108-KB_3O_5$  and  $mC72-KB_3O_5$  metastable structures, the coordination number of potassium in  $mP108-KB_3O_5$  is eight, which corresponds to lower energy. Therefore, we speculate that the average coordination number of potassium in structures with lower potassium content is about seven to eight, which is more conducive to the formation of lower energy configurations.

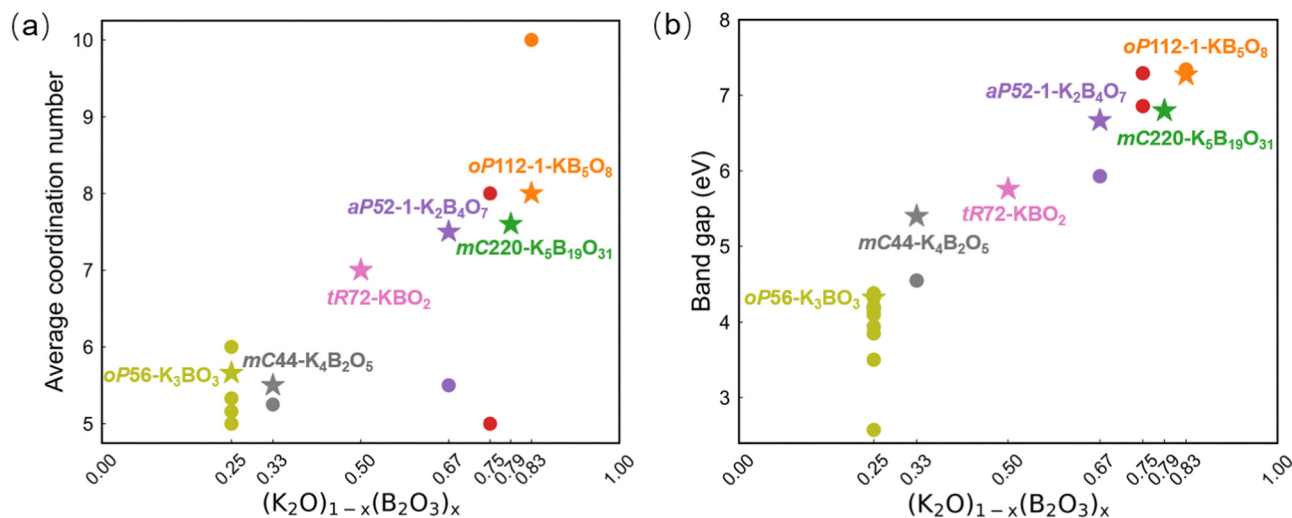


Fig. 3 (a) The average coordination number of potassium atoms in compounds. (b) Band gap values of all compounds (calculated using the HSE06 functional), where pentagrams represent the stable structures, dots represent metastable structures, and the same color indicates the same composition.

### 3.3 Electronic structures

The electronic structures fundamentally determine the physical and chemical properties of materials, thereby making them essential to conduct an in-depth study of the electronic structures in the  $K_2O-B_2O_3$  system. Recognizing that the GGA functional typically underestimates band gaps, we utilized the hybrid functional HSE06 for electronic structure calculations to obtain accurate band gaps. We have observed a correlation between the band gap values and compositions (Fig. 3b). With the increase in the  $B_2O_3$  content, there is also a gradual increment in the band gap values. Among all structures, *hP14-K<sub>3</sub>BO<sub>3</sub>* exhibits the smallest band gap, only 2.57 eV, corresponding to an absorption edge at 482 nm, thereby blocking ultraviolet light transmission. The absorption edges of the other structures are all located in the UV region. It is noteworthy that when the  $B_2O_3$  content exceeds 0.67, the bandgap value increases to over 6 eV, extending the absorption edges into the deep UV range.

It is known that the electronic states near the Fermi level determine the optical properties of the crystal. Therefore, we conducted a detailed analysis of the electronic states of each formula at the valence band maximum (VBM) and the conduction band minimum (CBM) in these structures. The projected density of states is depicted in Fig. 4 (stable structures) and Fig. S4 (ESI<sup>†</sup>). These diagrams showcase that the electrons occupying the highest energy level of the valence band

primarily originate from the p orbitals of oxygen atoms, followed by those of boron. The orbitals of oxygen and boron exhibit significant overlap, indicative of a covalent bonding interaction. For *oP56-K<sub>3</sub>BO<sub>3</sub>*, *mC44-K<sub>4</sub>B<sub>2</sub>O<sub>5</sub>*, and *tR72-KBO<sub>2</sub>*, the peaks at the valence band appear more localized and dispersed, featuring numerous unbonded oxygen atoms, whereas for the other ground state structures, the electron states show more continuous characteristics. For the lowest energy level of the conduction band, the primary contributions come from the s and p orbitals of the potassium atoms.

### 3.4 Optical properties

We calculated the birefringence of all structures in hopes of identifying birefringent crystal materials suitable for further experimental synthesis, thereby providing theoretical guidance for experimental work (Table 1). In the predicted fourteen structures, since *oP56-K<sub>3</sub>BO<sub>3</sub>* and *mC44-K<sub>4</sub>B<sub>2</sub>O<sub>5</sub>* respectively belong to the orthorhombic and monoclinic systems, they are biaxial crystals. The calculated birefringence values are 0.025@1064 nm and 0.032@1064 nm, respectively. However, the birefringence of these two ground state structures is relatively small, lacking distinct advantages when compared to other reported birefringent crystals. Crystal structures exhibiting a birefringence exceeding 0.05@1064 nm have been selected for

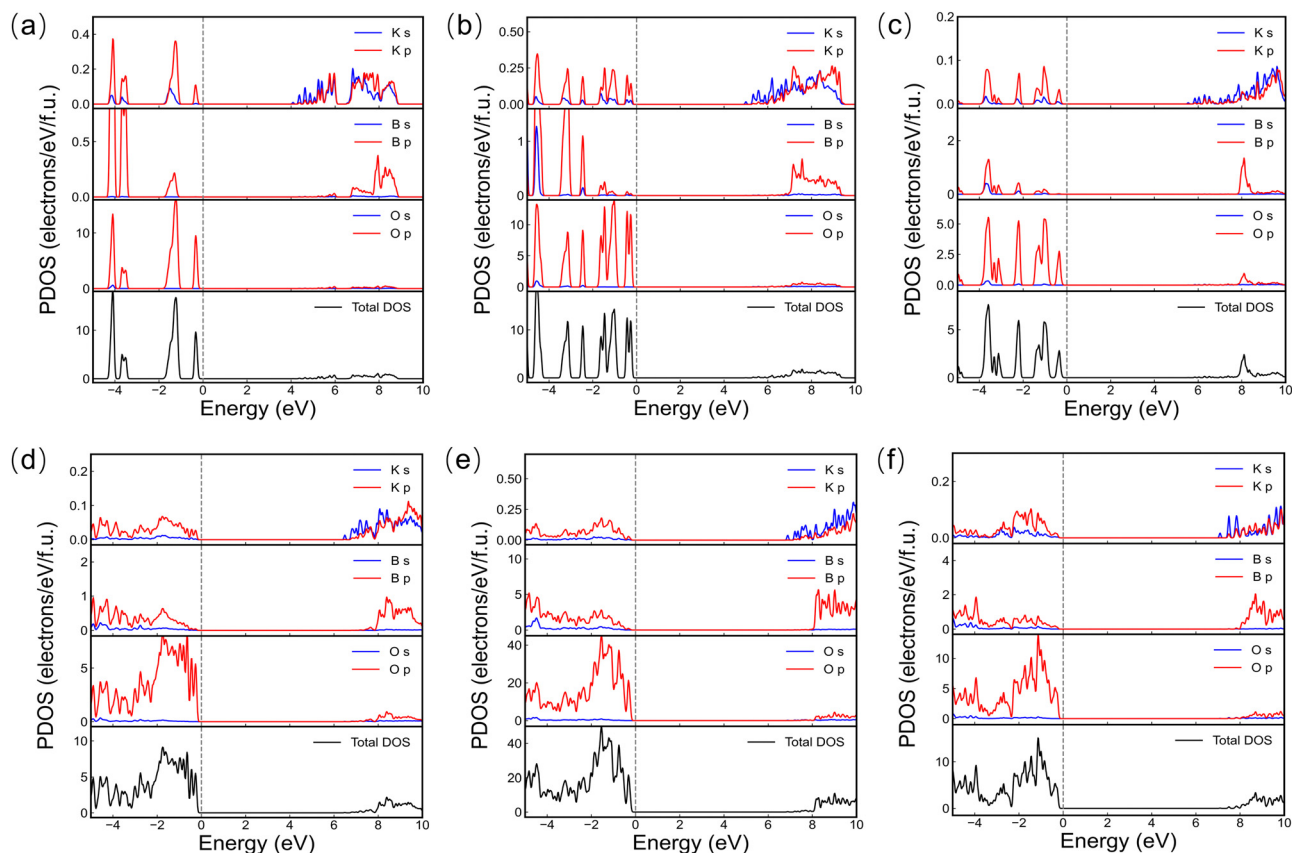


Fig. 4 Projected density of states, (a) *oP56-K<sub>3</sub>BO<sub>3</sub>*, (b) *mC44-K<sub>4</sub>B<sub>2</sub>O<sub>5</sub>*, (c) *tR72-KBO<sub>2</sub>*, (d) *aP52-1-K<sub>2</sub>B<sub>4</sub>O<sub>7</sub>*, (e) *mC220-K<sub>5</sub>B<sub>19</sub>O<sub>31</sub>*, and (f) *oP112-1-KB<sub>5</sub>O<sub>8</sub>*. The vertical dashed line represents the Fermi level.

**Table 1** Band gap, absorption edge, and birefringence of structures in the  $K_2O-B_2O_3$  system

	Bandgap (eV)	Absorption edge (nm)	Birefringence (@1064nm)
<i>oP56-K<sub>3</sub>BO<sub>3</sub></i>	4.32	287	0.025
<i>hR21-K<sub>3</sub>BO<sub>3</sub></i>	4.18	297	0.056
<i>mP28-1-K<sub>3</sub>BO<sub>3</sub></i>	4.16	298	0.053
<i>mP28-2-K<sub>3</sub>BO<sub>3</sub></i>	3.85	322	0.030
<i>hP14-K<sub>3</sub>BO<sub>3</sub></i>	2.57	482	0.059
<i>mP28-3-K<sub>3</sub>BO<sub>3</sub></i>	4.33	286	0.020
<i>mP28-4-K<sub>3</sub>BO<sub>3</sub></i>	4.38	283	0.009
<i>aP14-K<sub>3</sub>BO<sub>3</sub></i>	3.94	315	0.007
<i>aP28-1-K<sub>3</sub>BO<sub>3</sub></i>	3.50	354	0.033
<i>aP28-2-K<sub>3</sub>BO<sub>3</sub></i>	4.10	302	0.022
<i>mP28-5-K<sub>3</sub>BO<sub>3</sub></i>	4.27	290	0.016
<i>mC44-K<sub>4</sub>B<sub>2</sub>O<sub>5</sub></i>	5.40	230	0.032
<i>aP22-K<sub>4</sub>B<sub>2</sub>O<sub>5</sub></i>	4.55	273	0.011
<i>tR72-KBO<sub>2</sub></i>	5.76	215	0.096
<i>aP52-1-K<sub>2</sub>B<sub>4</sub>O<sub>7</sub></i>	6.67	186	0.028
<i>aP52-2-K<sub>2</sub>B<sub>4</sub>O<sub>7</sub></i>	5.93	209	0.025
<i>mP108-KB<sub>3</sub>O<sub>5</sub></i>	6.86	181	0.016
<i>mC72-KB<sub>3</sub>O<sub>5</sub></i>	7.29	170	0.032
<i>mC220-K<sub>5</sub>B<sub>19</sub>O<sub>31</sub></i>	6.90	179	0.05 <sup>28</sup>
<i>oP112-1-KB<sub>5</sub>O<sub>8</sub></i>	7.27	171	0.063
<i>oP112-2-KB<sub>5</sub>O<sub>8</sub></i>	7.34	169	0.069

detailed evaluation of their suitability as UV optical materials (Fig. 5).

The metastable structures *hR21-K<sub>3</sub>BO<sub>3</sub>*, *mP28-1-K<sub>3</sub>BO<sub>3</sub>*, and *hP14-K<sub>3</sub>BO<sub>3</sub>* exhibit moderate birefringence (Fig. 5a). These structures possess coplanar or nearly coplanar  $BO_3$  groups, which increase the polarizability differences in different directions, significantly contributing to their birefringence properties. In addition, *hP14-K<sub>3</sub>BO<sub>3</sub>* demonstrates the highest birefringence with a smaller bandgap, rendering it unsuitable for ultraviolet applications. *mP28-1-K<sub>3</sub>BO<sub>3</sub>* exhibits an absorption edge at 298 nm, suggesting its potential as a UV birefringent crystal.

Due to its non-centrosymmetric structure, *hR21-K<sub>3</sub>BO<sub>3</sub>* can generate second harmonic generation (SHG) effects. Further investigation into its nonlinear optical properties is warranted. The practical application of nonlinear optical materials relies on determining the phase-matching wavelength.<sup>57</sup> Phase matching<sup>57</sup> refers to the equality of wave vectors between

fundamental frequency radiation and second harmonic radiation, expressed as  $n(\omega) = n(2\omega)$ . The shortest phase-matching wavelength  $\lambda_{PM}$  is where the maximum refractive index at the fundamental wavelength  $\lambda$  is equivalent to the minimum refractive index at the double frequency wavelength  $\lambda/2$ , as shown in Fig. 5c. Its shortest phase-matching wavelength is 273 nm. Nevertheless, the calculated absorption edge is determined to be 297 nm, implying that light with a wavelength below 297 nm will be unable to transmit. In addition, second order polarizability tensor  $\chi_{ijk}^{(2)}(-2\omega, \omega, \omega)$ <sup>58,59</sup> describes the generation of the  $i$ -th component of the polarization at frequency  $2\omega$  in a medium, resulting from the interaction of two optical fields both at frequency  $\omega$ , with polarization directions  $j$  and  $k$ , respectively. By analyzing the imaginary part of the second-order susceptibility (Fig. S5, ESI<sup>†</sup>), we find that anisotropy in the linear optical properties is enhanced more significantly in the nonlinear spectra. A comparison at  $\omega$  and  $2\omega$  term profiles (interbands and intrabands) revealed that the contributions to the susceptibility from  $2\omega$  terms dominate the low energy regions whereas the high energy state is mixed with  $\omega$  and  $2\omega$  terms. These characteristics further highlight the relatively strong birefringence nature of *hR21-K<sub>3</sub>BO<sub>3</sub>*. And the biggest value of the second order susceptibility reaches 52.5 pm V<sup>-1</sup> at an energy of 3.64 eV (Fig. S6, ESI<sup>†</sup>). In experiments, the conversion efficiency of SHG is typically quantified using the nonlinear optical coefficient  $d_{il}$ .<sup>60</sup> Due to the symmetry between indices  $j$  and  $k$ , it follows that  $\chi_{ijk}^{(2)} = 2d_{il}^{(2)}$ . The calculated values for the frequency doubling components ( $\lambda = 1064$  nm) are as follows:  $d_{15} = d_{24} = -0.155$  pm V<sup>-1</sup>,  $d_{16} = d_{21} = -d_{22} = -1.775$  pm V<sup>-1</sup>,  $d_{31} = d_{32} = -0.15$  pm V<sup>-1</sup>, and  $d_{33} = -0.297$  pm V<sup>-1</sup>. As a result, the largest SHG coefficient is determined as 1.775 pm V<sup>-1</sup>, approximately 4.6 times the  $d_{36}$  of  $KH_2PO_4$  (KDP). In summary, *hR21-K<sub>3</sub>BO<sub>3</sub>* stands out as a potential UV nonlinear optical crystal.

Among the structures synthesized experimentally, *tR72-KBO<sub>2</sub>* exhibits 0D planar  $B_3O_6$  rings. This structural characteristic enhances the average anisotropy of polarizability and, being greater than that of separate  $BO_3$  groups, is more conducive to the formation of crystals with high birefringence. We use the hybrid functional to calculate the band gap to be

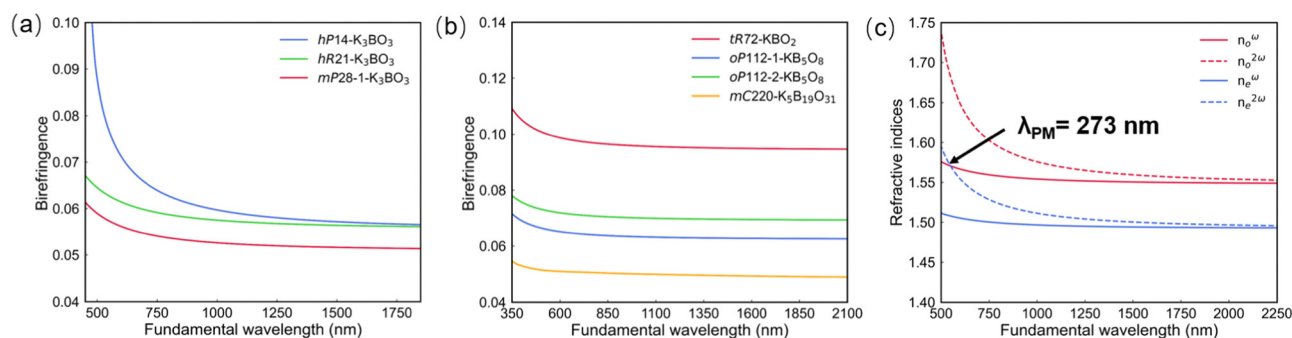


**Fig. 5** The calculated birefringence. We enumerate all structures with birefringence greater than 0.05@1064 nm. (a) Three predicted structures: *hP14-K<sub>3</sub>BO<sub>3</sub>*, *hR21-K<sub>3</sub>BO<sub>3</sub>*, and *mP28-1-K<sub>3</sub>BO<sub>3</sub>*. (b) Four experimentally synthesized structures: *tR72-KBO<sub>2</sub>*, *oP112-1-KB<sub>5</sub>O<sub>8</sub>*, *oP112-2-KB<sub>5</sub>O<sub>8</sub>*, and *mC220-K<sub>5</sub>B<sub>19</sub>O<sub>31</sub>*.<sup>28</sup> (c) Calculated shortest phase-matching wavelengths of *hR21-K<sub>3</sub>BO<sub>3</sub>*.

5.75 eV, and its corresponding absorption edge is 215 nm. Of great significance is the  $\text{KBO}_2$  crystal's substantial birefringence, estimated at 0.096@1064 nm and 0.1@564 nm, highlighting its crucial optical characteristics.

Moreover, the absorption edges of  $oP112-1\text{-KB}_5\text{O}_8$  and  $oP112-2\text{-KB}_5\text{O}_8$  are both located below 180 nm, and show larger birefringence, which are potential deep UV birefringent materials. These two structures exhibit similar structural features (Fig. 2), resulting in closely matched birefringence. This suggests that the spatial connections of the  $\text{B}_5\text{O}_{10}$  double rings also enhance the anisotropy of the structural polarization, with their contribution even exceeding that of the coplanar 0D  $\text{BO}_3$  groups.

## 4 Conclusions

In this study, we employed ionic substitutions and the evolutionary algorithm USPEX coupled with the first-principles calculation to explore the phase space of the pseudo-binary  $\text{K}_2\text{O-B}_2\text{O}_3$  system. Through structural prediction, fourteen novel structures have been successfully predicted, including two ground state structures ( $oP56\text{-K}_3\text{BO}_3$  and  $mC44\text{-K}_4\text{B}_2\text{O}_5$ ). We systematically investigated the electronic structures and optical properties of all structures to evaluate their potential application value and provide insights for experimental synthesis. The results indicate that  $mP28\text{-1-K}_3\text{BO}_3$  and  $tR72\text{-KBO}_2$  have been identified as potential UV birefringent materials. Notably,  $tR72\text{-KBO}_2$  exhibits significant birefringence (0.096@1064 nm), primarily attributed to the contribution of its parallel 0D  $\text{B}_3\text{O}_6$  units.  $mC220\text{-K}_5\text{B}_{19}\text{O}_{31}$ ,  $oP112\text{-1-KB}_5\text{O}_8$ , and  $oP112\text{-2-KB}_5\text{O}_8$ , with their wide band gaps ( $\sim 7$  eV), are considered potential candidates for deep UV birefringent applications. It is noteworthy that we also discovered the only non-centrosymmetric structure in this system,  $hR21\text{-K}_3\text{BO}_3$ . This structure demonstrates a significant frequency doubling coefficient ( $\sim 4.6$  KDP) and a moderate birefringence index (0.056@1064 nm), making it highly suitable for UV nonlinear optics applications. These discoveries not only enrich the diversity of borates but also expand the possibilities for optical material synthesis and design.

## Data availability

The data supporting this article have been included as part of the ESI.†

## Conflicts of interest

There are no conflicts to declare.

## Acknowledgements

The authors would like to thank Xiangyang Liu for carefully reading the manuscript. This work was supported by the National Science Fund for Excellent Young Scientist Fund

Program (Overseas) of China, the Science and Technology Activities Fund for Overseas Researchers of Shaanxi Province, China, and the Research Fund of the State Key Laboratory of Solidification Proceeding (NPU) of China (No. 2023-TS-15 and No. 2024-ZD-01). The calculations were supported by the International Center for Materials Discovery (ICMD) cluster of NPU.

## References

- Z. Guoqing, X. Jun, C. Xingda, Z. Heyu, W. Siting, X. Ke, D. Peizhen and G. Fuxi, *J. Cryst. Grow.*, 1998, **191**, 517–519.
- Z.-Y. Xie, L.-G. Sun, G.-Z. Han and Z.-Z. Gu, *Adv. Mater.*, 2008, **20**, 3601–3604.
- P. Hlubina, D. Ciprian and L. Knyblova, *Opt. Commun.*, 2006, **260**, 535–541.
- A. Tudi, S. Han, Z. Yang and S. Pan, *Coord. Chem. Rev.*, 2022, **459**, 214380.
- N. Tuerhong, H. Chen, M. Hu, X. Cui, H. Duan, Q. Jing and Z. Chen, *Phys. Chem. Chem. Phys.*, 2024, **26**, 15751–15757.
- X. Chen, B. Zhang, F. Zhang, Y. Wang, M. Zhang, Z. Yang, K. R. Poeppelmeier and S. Pan, *J. Am. Chem. Soc.*, 2018, **140**, 16311–16319.
- C. Jin, F. Li, B. Cheng, H. Qiu, Z. Yang, S. Pan and M. Mutailipu, *Angew. Chem.*, 2022, **134**, e202203984.
- R. Yang, A. Tudi, Y. Dang, K. Zhang and H. Shi, *Phys. Chem. Chem. Phys.*, 2023, **25**, 18646–18651.
- M. J. Dodge, *Appl. Opt.*, 1984, **23**, 1980–1985.
- S. Wu, G. Wang, J. Xie, X. Wu, Y. Zhang and X. Lin, *J. Cryst. Grow.*, 2002, **245**, 84–86.
- G. Zhou, J. Xu, X. Chen, H. Zhong, S. Wang, K. Xu, P. Deng and F. Gan, *Current Developments in Optical Elements and Manufacturing*, 1998, pp. 15–19.
- R. Appel, C. D. Dyer and J. N. Lockwood, *Appl. Opt.*, 2002, **41**, 2470–2480.
- M. Mutailipu, K. R. Poeppelmeier and S. Pan, *Chem. Rev.*, 2020, **121**, 1130–1202.
- J. Min, A. Abudurusuli, J. Li, S. Pan and Z. Yang, *Phys. Chem. Chem. Phys.*, 2020, **22**, 19697–19703.
- Y. Yang, S. Pan, X. Hou, C. Wang, K. R. Poeppelmeier, Z. Chen, H. Wu and Z. Zhou, *J. Mater. Chem.*, 2011, **21**, 2890–2894.
- F. Zhang, X. Chen, M. Zhang, W. Jin, S. Han, Z. Yang and S. Pan, *Light: Sci. Appl.*, 2022, **11**, 252.
- M. Zhang, D. An, C. Hu, X. Chen, Z. Yang and S. Pan, *J. Am. Chem. Soc.*, 2019, **141**, 3258–3264.
- X. Wang, Y. Wang, B. Zhang, F. Zhang, Z. Yang and S. Pan, *Angew. Chem.*, 2017, **129**, 14307–14311.
- Y. Wang, E. Tikhonov and H. Niu, *Chem. Mater.*, 2023, **35**, 4201–4210.
- W. Zachariasen, *J. Chem. Phys.*, 1937, **5**, 919–922.
- W. Schneider and G. Carpenter, *Acta Crystallogr., Sect. B: Struct. Crystallogr. Cryst. Chem.*, 1970, **26**, 1189–1191.
- R. Bubnova, V. Fundamenskii, S. Filatov and I. Polyakova, *Dokl. Phys. Chem.*, 2004, 249–253.

- 23 S. C. Neumair, S. Vanicek, R. Kaindl, D. M. Töbrens, C. Martineau, F. Taulelle, J. Senker and H. Huppertz, *Eur. J. Inorg. Chem.*, 2011, 4147–4152.
- 24 J. Krogh-Moe, *Acta Crystallogr., Sect. B: Struct. Crystallogr. Cryst. Chem.*, 1972, **28**, 3089–3093.
- 25 J. Krogh-Moe, *Acta Crystallogr.*, 1965, **18**, 1088–1089.
- 26 J. Krogh-Moe, *Acta Crystallogr., Sect. B: Struct. Crystallogr. Cryst. Chem.*, 1972, **28**, 168–172.
- 27 J. Krogh-Moe, *Acta Crystallogr., Sect. B: Struct. Crystallogr. Cryst. Chem.*, 1974, **30**, 1827–1832.
- 28 S. Huang, C. Zhou, S. Cheng and F. Yu, *ChemistrySelect*, 2019, **4**, 10436–10441.
- 29 C. Chen, Y. Wu and R. Li, *Int. Rev. Phys. Chem.*, 1989, **8**, 65–91.
- 30 C.-T. Chen, *Acta Phys. Sin.*, 1976, **25**, 146–161.
- 31 X. Zhou, J. Huang, G. Cai, H. Zhou, Y. Huang and X. Su, *Dalton Trans.*, 2020, **49**, 3284–3292.
- 32 G. Hautier, C. Fischer, V. Ehlacher, A. Jain and G. Ceder, *Inorg. Chem.*, 2011, **50**, 656–663.
- 33 C. W. Glass, A. R. Oganov and N. Hansen, *Comput. Phys. Commun.*, 2006, **175**, 713–720.
- 34 A. O. Lyakhov, A. R. Oganov, H. T. Stokes and Q. Zhu, *Comput. Phys. Commun.*, 2013, **184**, 1172–1182.
- 35 S. Zhang, Q. Yang, X. Zhang, K. Zhao, H. Yu, L. Zhu and H. Liu, *Phys. Chem. Chem. Phys.*, 2021, **23**, 21544–21553.
- 36 S. P. Ong, W. D. Richards, A. Jain, G. Hautier, M. Kocher, S. Cholia, D. Gunter, V. L. Chevrier, K. A. Persson and G. Ceder, *Comput. Mater. Sci.*, 2013, **68**, 314–319.
- 37 G. Kresse and J. Furthmüller, *Phys. Rev. B: Condens. Matter Mater. Phys.*, 1996, **54**, 11169.
- 38 J. P. Perdew, J. A. Chevary, S. H. Vosko, K. A. Jackson, M. R. Pederson, D. J. Singh and C. Fiolhais, *Phys. Rev. B: Condens. Matter Mater. Phys.*, 1992, **46**, 6671.
- 39 J. P. Perdew, K. Burke and M. Ernzerhof, *Phys. Rev. Lett.*, 1996, **77**, 3865.
- 40 E. Zintl, A. Harder and B. Dauth, *Z. Elektrochem. Angew. Phys. Chem.*, 1934, **40**, 588–593.
- 41 H. Effenberger, C. L. Lengauer and E. Parthé, *Monatsh. Chem.*, 2001, **132**, 1515–1517.
- 42 A. Togo, F. Oba and I. Tanaka, *Phys. Rev. B: Condens. Matter Mater. Phys.*, 2008, **78**, 134106.
- 43 K. Momma and F. Izumi, *J. Appl. Crystallogr.*, 2011, **44**, 1272–1276.
- 44 A. V. Krukau, O. A. Vydrov, A. F. Izmaylov and G. E. Scuseria, *J. Chem. Phys.*, 2006, **125**, 224106.
- 45 X. Gonze, B. Amadon, P.-M. Anglade, J.-M. Beuken, F. Bottin, P. Boulanger, F. Bruneval, D. Caliste, R. Caracas and M. Côté, *et al.*, *Comput. Phys. Commun.*, 2009, **180**, 2582–2615.
- 46 D. Hamann, *Phys. Rev. B: Condens. Matter Mater. Phys.*, 2013, **88**, 085117.
- 47 V. Fiorentini and A. Baldereschi, *Phys. Rev. B: Condens. Matter Mater. Phys.*, 1995, **51**, 17196.
- 48 W. Sun, S. T. Dacek, S. P. Ong, G. Hautier, A. Jain, W. D. Richards, A. C. Gamst, K. A. Persson and G. Ceder, *Sci. Adv.*, 2016, **2**, e1600225.
- 49 A. R. Oganov, C. J. Pickard, Q. Zhu and R. J. Needs, *Nat. Rev. Mater.*, 2019, **4**, 331–348.
- 50 M. Mutailipu, K. R. Poepelmeier and S. Pan, *Chem. Rev.*, 2020, **121**, 1130–1202.
- 51 D. F. Eaton, *Science*, 1991, **253**, 281–287.
- 52 H. Fan, N. Ye and M. Luo, *Acc. Chem. Res.*, 2023, **56**, 3099–3109.
- 53 A. Reshak, *Phys. Chem. Chem. Phys.*, 2017, **19**, 30703–30714.
- 54 J. E. Saal, S. Kirklin, M. Aykol, B. Meredig and C. Wolverton, *JOM*, 2013, **65**, 1501–1509.
- 55 S. Kirklin, J. E. Saal, B. Meredig, A. Thompson, J. W. Doak, M. Aykol, S. Rühl and C. Wolverton, *npj Comput. Mater.*, 2015, **1**, 1–15.
- 56 J. Schmidt, N. Hoffmann, H.-C. Wang, P. Borlido, P. J. Carriço, T. F. Cerqueira, S. Botti and M. A. Marques, *arXiv*, 2022, preprint, arXiv:2210.00579, DOI: [10.48550/arXiv.2210.00579](https://doi.org/10.48550/arXiv.2210.00579).
- 57 W. Zhang, H. Yu, H. Wu and P. S. Halasyamani, *Chem. Mater.*, 2017, **29**, 2655–2668.
- 58 C.-G. Duan, J. Li, Z.-Q. Gu and D.-S. Wang, *Phys. Rev. B: Condens. Matter Mater. Phys.*, 1999, **60**, 9435.
- 59 G. Guo, K. Chu, D.-S. Wang and C.-G. Duan, *Phys. Rev. B: Condens. Matter Mater. Phys.*, 2004, **69**, 205416.
- 60 D. A. Kleinman, *Phys. Rev.*, 1962, **126**, 1977.